

Cite this: *Soft Matter*, 2012, **8**, 10641

www.rsc.org/softmatter

PAPER

## Microfluidic wet-spinning of alginate microfibers: a theoretical analysis of fiber formation

Oriane Bonhomme,<sup>\*abc</sup> Jacques Leng<sup>abc</sup> and Annie Colin<sup>abc</sup>

Received 9th March 2012, Accepted 29th May 2012

DOI: 10.1039/c2sm25552a

We investigate the conditions under which fibers can be fabricated in a microfluidic chip upon gelation of alginate with a calcium salt. We develop a device which permits us to generate a perfectly centered axial coflow and we study the influence of control parameters, namely the salt concentration, the residence time, and the size of the polymeric jet, on the gelation process. We monitor several states which include no gel, continuous fibers, pieces of gel and clogging. To describe the resulting state diagrams, we develop a model of reaction–diffusion under flow which permits us to estimate the density of links created during the gelation. While the no-gel and clogging states are chiefly governed by the density of links (respectively very low and very high), the selection of fibers against pieces-of-gel is controlled by the stress exerted on the jet at the level of the injection nozzle, also called spinneret. This simple modeling of conditions required to create fibers as an interplay between gel strength and local elongational stress might be useful for the fabrication and miniaturization of functional fibers.

### 1 Introduction

Submillimetric monodisperse particles and fibers are technical objects that are useful in many realms such as drug delivery<sup>1,2</sup> or tissue engineering,<sup>3–5</sup> and micro- and millifluidics have proven extremely powerful techniques for their synthesis.<sup>6</sup> Not only are these techniques continuous processes but because they operate at a small scale, all transport properties are well mastered, which includes an excellent control over the flow of matter and heat. Most of the achievements in particle fabrication also exploit the possibility to control the wetting properties inside the micro-devices along with the confinement. Indeed, thanks to a Rayleigh–Plateau instability in a confined geometry,<sup>7</sup> two-phase flows of immiscible fluids offer a bottom-up route to emulsification and encapsulation. The formation of calibrated drops is reproducible and controllable with the operating parameters such as flow rates, viscosities, and surfactant concentrations and beautiful structures have been produced: monodisperse emulsions, double emulsions,<sup>8</sup> vesicles<sup>9,10</sup> or polymersomes,<sup>11,12</sup> etc. The subsequent use of *in situ* solidification *via* photopolymerization appears to be a simple and cost-effective way to produce uniformly sized hard particles (microparticles, microstrips, microcapsules and also fibers<sup>13–15</sup>). This fabrication procedure leads to a reasonable yield but a strong limitation comes from the use of specific photocurable polymers. Although

more difficult to implement, sol–gel reactions are interesting alternatives for the *in situ* solidification of the structures.

The fabrication of fibers in microfluidic devices has been recently studied. Fibers are shaped up by coflowing two miscible fluids and the shape is then frozen. In industrial wet-spinning, the external fluid also serves as a coagulating bath for freezing the shape, but for the microfluidic approach any solidification technique appears adequate: gelation of a polymer based on the diffusion of a cross-linker,<sup>16–21</sup> solvent exchange for precipitating a polymer,<sup>22</sup> or on-the-fly photopolymerization.<sup>15,23</sup> We note however that stringent conditions must be met in order to obtain in-line solidification: molecular diffusion of the inner material (that will make the fiber) must be limited in order to preserve the shape whereas cross-linking must be fast enough to take place inside the chip; yet, if too fast, blockages and clogging may also happen, along with shape instabilities such as buckling. All these transport phenomena are related, depend on the flow rates, molecular diffusion and chemical kinetics, and a subtle interplay must be found in order to obtain fibers. At this stage, the conditions required to obtain fibers are not rationalized. A quantitative description of the reaction diffusion mechanism in charge of the fiber formation is still lacking.

In order to address this issue, we first explore experimentally the flow diagrams obtained in an axial microfluidic coflow of a polymer solution (alginate) and a solution of its cross-linker (calcium salt). We depict the flow behavior and the objects we obtained as a function of the residence time in the microfluidic chip, the ratio of flow rates and the salt concentration which are three *independent and relevant* variables of the problem of gelation under flow. Such a diagram displays several zones. They include no gel, two types of fibers (size tunable with flow-rate or

<sup>a</sup>Univ. Bordeaux, LOF, UMR 5258, F-33600 Pessac, France. E-mail: oriane.bonhomme.ob@gmail.com

<sup>b</sup>CNRS, LOF, UMR 5258, F-33600 Pessac, France

<sup>c</sup>RHODIA, LOF, UMR 5258, F-33600 Pessac, France

not), discontinuous fibers (monodisperse pieces of gel that have not been reported previously in the literature) and clogging. We note that the region in which tunable fibers exist is fine yet reproducible. The second main originality of our work is to quantify these observations. To do so, we solve the diffusion–reaction kinetics under flow with a set of important hypotheses. The steady-state flow pattern is calculated with the Stokes equation; we neglect the diffusion of the polymer but account for that of the salt (cross-linker) which induces the gelation described as a precipitation-like reaction with a solubility product. It permits us to calculate everywhere and at any times all the concentration fields in the flow (polymer, salt, and gel) from which we evaluate the bond density created locally in the gel. We use it to evaluate the ability of the gel to bear an elongational stress at the level of the spinneret (or nozzle, *i.e.*, the junction of the two-level channels). Within this description, we can sort all the zones observed experimentally in the flow diagram as a function of the bond density and the elongational stress: there is no gel below the solubility product and clogging occurs at very high density of links; pieces-of-gel and tunable fibers occur both at a moderate link density and the sign of the elongational stress at the level of the nozzle is a very good indicator of the selected shape. The use of this approach will allow in the future the choice of control parameters for fiber production.

## 2 Materials and methods

### 2.1 Chemicals

The alginate is purchased from Sigma-Aldrich (A-2033) and we prepare solutions at 2 wt% in deionized water. As the properties of this alginate are not given by the supplier, we measure its flow curve in a stress-controlled rheometer in cone–plate geometry and evidence a strong shear-thinning behavior where the viscosity  $\eta_i$  varies like  $\eta_i = 8.96\dot{\gamma}^{-0.47}$  with the shear-rate  $\dot{\gamma}$ . The literature indicates a molecular weight around  $3.3 \times 10^7 \text{ g mol}^{-1}$  and a proportion between guluronic (G) and mannuronic (M) acid groups of 1.86 (ref. 24 and 25).

Anhydrous calcium chloride comes from Fisher.

Solutions are prepared with Millipore water.

### 2.2 Microfluidic chip for aligned coflows

We intend to create axial coflows with a core–shell geometry and developed a microfluidic device which is able to generate a near-perfect cylindrical coflow. Indeed, we found that nested-capillary chips<sup>9</sup> show in general a slight misalignment which is deleterious to the fabrication of fibers. Hybrid devices<sup>16,26</sup> appear more adequate but as they involve at least one step of photolithography; we chose an all-PDMS version inspired by a recent development of *cylindrical* capillaries obtained with PDMS.<sup>18</sup>

First, we fabricate with photolithography (SU8 resist on a silicon wafer) a two-level master on which we create two sets of patterns of different heights that will later make up the fluidic channels. We then replicate this mold twice in PDMS and stick the two slabs face-to-face, thereby creating the channels. Fig. 1 shows such a PDMS chip with a close-up and a simple scheme highlighting the geometry of the spinneret. A critical step is the alignment of the two slabs; it can be done under a microscope in order to obtain a near-perfect geometry (within a few microns).

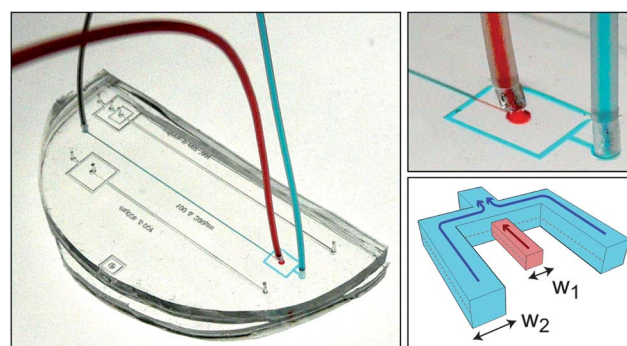


**Fig. 1** Two views of the PDMS chip that generates an axial, self-centered coflow. The scheme at the bottom right illustrates the geometry of channels obtained by sticking face-to-face the two halves, *i.e.*, identical slabs molded on a two-level photolithographed master ( $w_1 = 100 \mu\text{m}$ ,  $w_2 = 400 \mu\text{m}$ ).

When successful, we obtain self-centered, perfectly aligned capillaries with a *square basis* and two widths (100 and 400  $\mu\text{m}$  in our case). Unlike the demonstration chip of Fig. 1, we cut the PDMS slab perpendicular to the channels at the level of the outlet in order to leave it free of tubings: it is actually the collection part of the gelled polymers and we wish to minimize shear or elongational stress effects at this level. The length of the device is  $L_{\text{chip}} = 3 \text{ cm}$ .

### 2.3 Flow control

We use this PDMS chip to generate a cylindrical coflow with a core–shell structure where the polymer solution is injected in the core (inner fluid) and the calcium salt solution (external fluid) in the shell flow. The microfluidic chip is held vertically to bypass all sedimentation effects and the flow rate of each fluid is controlled independently with precision syringe-pumps (Nemesis by Cetoni).

Importantly, we use a set of four syringes in order to control the flow. Indeed, as we study a gelation dynamics which occurs nearly immediately after the salt solution has been brought into contact with the polymer solution, blockages inevitably occur during the transient state long before the steady flow has settled in. It clogs the flow and prevents further studies. In order to bypass this problem, we control the composition of the external fluid by mixing *before injection* a solution of calcium salt (concentration  $c_0$ , flow rate  $Q_{\text{salt}}$ ) with pure water (flow rate  $Q_{\text{water}}$ ). The mixing is performed in a home-made magnetic milli-stirrer. The actual salt concentration is thus *tunable* and reads  $c_{\text{salt}} = c_0 Q_{\text{salt}} / (Q_{\text{salt}} + Q_{\text{water}})$ . In practice, we keep the overall external flow rate,  $Q_e = Q_{\text{salt}} + Q_{\text{water}}$ , constant and initiate the flow *with pure water*. Only once the flow is steady do we turn to the desired salt concentration by tuning the ratio  $Q_{\text{salt}}/Q_{\text{water}}$  (while keeping the sum of the flow rates constant). The reverse action is also operated to stop the flow. We inject the inner solution at a flow rate  $Q_i$  and we can choose to inject either pure water or the polymer solution thanks to a 2-way valve in order to rinse the device when blockages occur. Fig. 2 illustrates this setup alongside a sketch of the flow pattern expected downstream the channel.

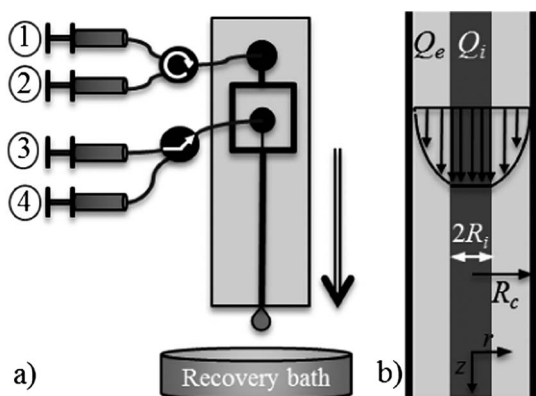


**Fig. 2** (a) Sketch of the experimental setup: the microfluidic device is held vertically and the fluids are injected at a controlled flow rate; solutions of syringes 1 (pure water) and 2 (calcium solution) are mixed within a magnetic milli-stirrer prior to injection in order to control the actual calcium composition. The inner fluid is selected *via* a valve and consists of either the alginate solution (syringe 3) or pure water (syringe 4) in order to rinse the device in the (frequent) case of clogging. (b) Sketch of the coflow in the microfluidic chip with the inner fluid (flow rate  $Q_i$ ) extending over  $2R_i$  and the external one (flow rate  $Q_e$ ) flowing in the channel of width  $2R_c$ . Note that the plug profile flow in the central part is only due to the very high value of the viscosity of the internal fluid.

For all experiments reported in the present article, we used a calcium salt solution in water at  $c_0 = 0.1\%$  in weight, and an alginate solution in water at  $2\%$  in weight.

## 2.4 Control parameters

The basics of a gelation experiment consist in cross-linking the flowing inner polymeric jet upon transverse molecular diffusion of the calcium ions. It is thus clear that the operational parameters of our experiment are interrelated: given a chip geometry (length  $L_{\text{chip}}$ , width  $2R_c$ ), the flow conditions are tuned with the flow rates  $Q_e$  and  $Q_i$  and select both the residence time and the dimension of the inner jet  $R_i$ ; the latter dimension is of crucial importance for the transverse diffusion; the bare salt concentration ( $c_0$ ) and the alginate concentration will also control the cross-linking process.

Therefore, we choose to reduce these parameters to a minimal set which encompasses all the phenomena: the salt concentration  $c_{\text{salt}}$ , the flow rate ratio  $r_Q$ , and the residence time  $t_{\text{res}}$ , which are defined with

$$c_{\text{salt}} = c_0 \frac{Q_{\text{salt}}}{Q_{\text{salt}} + Q_{\text{water}}}, \quad (1)$$

$$r_Q = \frac{Q_i}{Q_{\text{salt}} + Q_{\text{water}}}, \quad (2)$$

$$t_{\text{res}} = \frac{\pi L_{\text{chip}} R_i^2}{Q_i}. \quad (3)$$

In the rest of this work, we fix some of these variables. We keep the dimensions of the chip constant ( $L_{\text{chip}} = 3 \text{ cm}$ ,  $R_c = 200 \mu\text{m}$ ). The concentration of the polymeric jet is also kept constant ( $c_{\text{alg}} = 2 \text{ wt}\%$ ). As discussed above, the salt concentration can be varied with the flow rates  $Q_{\text{water}}$  and  $Q_{\text{salt}}$ , eqn (1).

Eventually, the residence time is defined with the mean velocity of the jet.

## 2.5 Observation techniques

We perform on-line and off-line observations.

The flow pattern is observed on-chip at several locations, typically close to the nozzle and close to the outlet, with a microscope equipped with an epifluorescence contrast and a fast camera. We add to the alginate solution fluorescent microparticles ( $\approx 10^{-3} \text{ vol}\%$  of  $1 \mu\text{m}$  diameter yellow-green fluorospheres by Invitrogen) which act as flow tracers.

We also collect the fluid at the outlet on a microscope glass slide and monitor the microstructures under a stereomicroscope equipped with bright-field, dark-field, and phase contrasts.

## 3 Experimental observations

We report first the microstructures obtained under flow and observed off-line, and from these observations we construct a state diagram describing the microstructure against the control parameters. We then give a local view of the flow which permits us to unveil some of the mechanisms involved in the microstructure formation.

### 3.1 Off-line observation and state diagram

There are many instances where we collect no gel at all *at the outlet* of the device and two situations actually lead to this lack of gel: it happens presumably when the gelation does not occur in the device (for example when the concentration of gelling agent is too small, *i.e.*, when some solubility product is not reached) or when the gelation is so strong that it blocks the flow.

When a gel is created, it may take two distinct shapes: continuous or discontinuous fibers (Fig. 3). On the left side of this figure, we see a gel with a very high aspect ratio and a quite constant section: it is a *continuous fiber*. On the right part, we observe slightly elongated chunks of gel with a very specific shape. These pseudo-rods are monodisperse, yet their geometry (length and diameter) can be tuned with the control parameters. We will call these microstructures *pieces-of-gel* in the following and we will show below that they originate from the regular (near-periodic) detachment of a gel that occurred at the level of the spinneret.

We represent these states in a diagram which is, in principle, three-dimensional due to the three control parameters

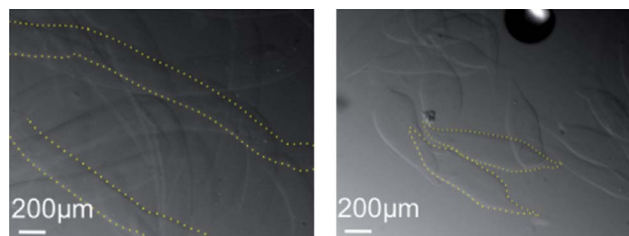


**Fig. 3** Micrographs of two types of gels obtained in the microfluidic spinneret (dark-field contrast): (left) continuous fibers and (right) pieces of fiber. In both cases, we highlighted the shape with a dotted line to enhance the view.

( $c_{\text{salt}}$ ,  $t_{\text{res}}$ ,  $r_Q$ ). For practical reasons, we represent the data at fixed  $r_Q$  (actually grouped over a limited range of  $r_Q$  values) and plot the state of the microstructure in the plane ( $c_{\text{salt}}$ ,  $t_{\text{res}}$ ), see Fig. 4.

It appears that on all these diagrams, the different microstructures are grouped in fairly well-defined zones. At very low salt concentration, gelation never occurs whatever the residence time (+ on Fig. 4). When the gelling agent is introduced with a higher concentration in the external layer, a gel is created in the chip. When the flow is fast, *i.e.*, small residence time, fibers are obtained (★); when the residence time is increased, pieces-of-gel are created (○). These diagrams also show that the border between fibers and pieces-of-gel corresponds to a smaller residence time when the salt concentration increases. When there is simultaneously a high salt concentration and a long residence time, a blockage appears (not shown on the diagrams, × in the following). Eventually, the location of the borders between these

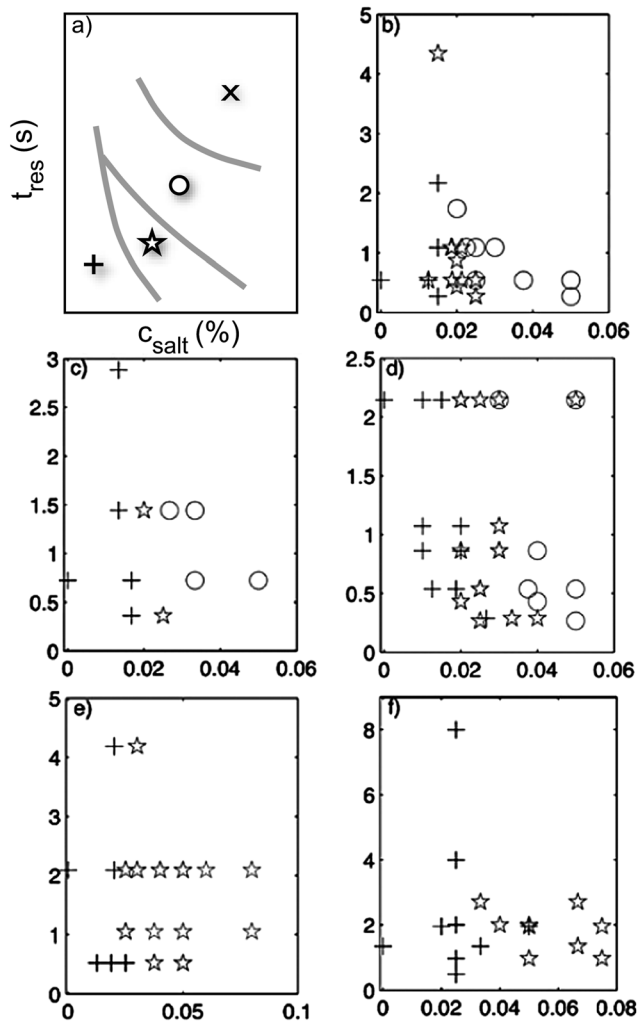


**Fig. 4** State diagrams of alginate gelation under flow in the ( $c_{\text{salt}}$ ,  $t_{\text{res}}$ ) coordinates: (a) is a schematic diagram showing all the states (+ for the absence of gel, ★ for continuous fibers, ○ for pieces of gel, × for blockage). (b–f) are experimental diagrams for several sizes of the inner jet: (b)  $0.02 < r_Q < 0.025$ , (c)  $0.03 < r_Q < 0.035$ , (d)  $0.04 < r_Q < 0.035$ , (e)  $0.1 < r_Q < 0.13$ , and (f)  $r_Q > 0.13$ .

zones also depends on the flow rate ratio, the larger the flow rate ratio, the wider the zone of fibers. As the radius of the wet fiber decreases with the flow rate ratio (see the Discussion), this suggests that very small fibers will be very difficult to obtain.

### 3.2 On-line observations

The observation of the flow pattern during gelation helps us to understand the microstructure formation. To better view the flow, we actually not only add tracers to the alginate but also a dye (Rhodamine 6G) that permits us to visualize the inner jet.

We illustrate first the aspect of the flow in the zone of *continuous fibers* in the state diagram. The flow is monitored in the middle of the chip (about 2 cm from the nozzle) and we observe that the jet does not look fluid at all; instead, it does not flow straight and exhibits plies. Fig. 5 (left a–e) displays a time-lapsed sequence of the flow with images cropped to the size of the external channel. Such an observation suggests a solid-like flow for the inner jet which underwent bending or buckling. Interestingly, we can induce this “buckling” instability by setting the flow conditions from *no gel* to *continuous fiber* (by increasing  $c_{\text{salt}}$  for instance) and we see that the shape oscillation starts from the outlet of the device and goes upstream, up to a distance which depends on the flow conditions. The frequency and the amplitude of the shape oscillations are also a function of the flow conditions.

To highlight the formation of the pieces-of-gel, we monitor the flow at the level of the injection nozzle. Again, a time-lapsed sequence is given (right part of Fig. 5) and we actually observe that the gel is created directly at the nozzle. In the first frame of the sequence, the inner jet is focused yet, in the successive frames (b–d), the radial extent of the jet in the focusing regions grows. Actually, gelation which takes place here as evidenced by some tracers that stay very long at the same position, freezes partially the shape but the jet is still fed by a polymer stream, so it grows. Soon after (e and f), the gel is pinched off, is carried away by the flow and one recovers a focused jet (g and h). This kinetics repeats itself and leads to the formation of pieces of gel whose shape can be understood on the basis of the pinching mechanism. We also note that under certain conditions, for instance when  $c_{\text{salt}}$  is too high, the viscous drag is not sufficient to tear off the gel: a blockage occurs and clogs the chip.

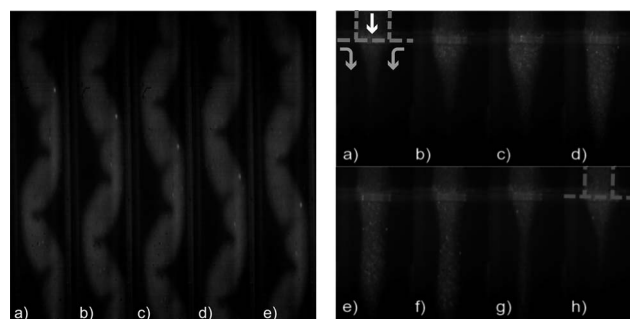


**Fig. 5** On-line observations of some gelation events using fluorescence (flow tracers + dye in the alginate jet). (Left) Time-sequence of the oscillations of the jet when fibers are produced; observation about 2 cm from the nozzle. (Right) Time-sequence of the gelation at the nozzle with a pinching dynamics that tears off the gel and leads to pieces of gel.

## 4 Reaction–diffusion under flow: a numerical analysis

### 4.1 The model

We now develop a simple model in order to understand these effects. We couple a simplified description of the longitudinal flow (along  $z$ ) to a radial reaction–diffusion mechanism (along  $r$ ) which describes the kinetics of gelation. We solve this reaction under flow numerically and obtain cartographies of the concentrations in the chip for all the species we consider, namely the polymer, the cross-linker, and the reticulated polymer. It yields a quantitative description of the gel build-up kinetics which we relate to the mechanical stress the material experiences locally. Such a simplified model permits us to rationalize and sort the different morphologies we observe experimentally. For the sake of simplicity, in the following we will calculate the velocity field and the concentration field in cylindrical geometry, which permits us to deal with an analytical solution of the velocity field. We are interested in the concentration profiles  $A(r, \theta, z)$ ,  $S(r, \theta, z)$  and  $G(r, \theta, z)$  of the alginate, salt and gel species. By symmetry, the flow field and the concentration fields do not depend upon  $\theta$ . Given our microfluidic motivation, we consider that the flow is strictly laminar (small Reynolds number) and that the species only disperse by molecular diffusion. After an entrance region of order  $\approx 3Rc$  from the junction, the flow takes the form  $\vec{v}(r, \theta, z) = v_z(r, z)\vec{e}_z$ . With these assumptions, the steady-state in the channel is described by:

$$\begin{cases} \vec{\nabla} \cdot \vec{v} = 0, \\ \vec{\nabla} P = \vec{\nabla} \cdot \underline{\underline{\sigma}}, \\ v_z(r, z) \partial_z [S] = D_S \left( \frac{1}{r} \partial_r (r \partial_r [S]) + \partial_z^2 [S] \right) + R_S, \\ v_z(r, z) \partial_z [A] = D_A \left( \frac{1}{r} \partial_r (r \partial_r [A]) + \partial_z^2 [A] \right) + R_A, \\ v_z(r, z) \partial_z [G] = D_G \left( \frac{1}{r} \partial_r (r \partial_r [G]) + \partial_z^2 [G] \right) + R_G, \end{cases} \quad (4)$$

where  $\vec{v}$  is the velocity,  $P$  is the pressure,  $\underline{\underline{\sigma}}$  is the deviator of the stress tensor,  $R_S$ ,  $R_A$ , and  $R_G$  are the reaction terms and  $D_S$ ,  $D_A$ , and  $D_G$  are the salt, the alginate and the gel diffusion coefficient respectively. The first two equations are used to calculate the velocity field while the three others really characterize the diffusion–reaction under flow.

To model the reaction terms, we now detail the gelation reaction. It involves *specific* carboxylic acid groups along the polymer chain which contains guluronic and mannuronic acids; only the former participates in the binding of  $\text{Ca}^{2+}$  ions into the gel whose topology has been described using the *egg box* model,<sup>27</sup> its maximum binding capacity is  $3/4 \text{ Ca}^{2+}$  per guluronic acid. To model the reaction term  $R$ , we thus use an *effective* reaction where all the acids are involved but a stoichiometric coefficient weights the possibility of links:



where  $\text{COO}^-$  corresponds to the totality of the acids involved in the solution. The coefficient  $n$  is therefore calculated according to the composition of the alginate (only the acids belonging to the

guluronic family are counted), its molecular weight, and the gelation model, *i.e.*, here the egg box model. We find  $n \approx 3.42$ , in agreement with ref. 28. We further assume that the gel formation is a precipitation-like reaction: a given amount of salt is required to initiate gelation and above this point, the unbound reactants are linked by a *solubility product* which fixes their concentrations. Beside, the kinetics is instantaneous and equilibrated. Above the gelation point, the free  $\text{COO}^-$  groups and the free  $\text{Ca}^{2+}$  ions concentrations, respectively noted  $[A]$  and  $[S]$  in the following, are linked by the solubility product  $K_s = [A]^n[S]$ . We also call  $[G]$  the concentration of created links. This reaction is characterized by an amount of matter  $\xi$  that is consumed and calculated as follows:

$$\begin{cases} \text{if } [A]^n[S] < K_s, \xi = 0, \\ \text{if } [A]^n[S] \geq K_s, \xi \text{ such as } ([A] - n\xi)^n([S] - \xi) = K_s. \end{cases} \quad (6)$$

$\xi$  is linked to the reaction terms by:  $R_S = -\xi$ ,  $R_A = -n\xi$ ,  $R_G = \xi$ .

### 4.2 The hypothesis of high Péclet number

To solve these equations, we proceed by assumptions. We first invoke our cylindrical geometry, *i.e.*  $r/L \ll 1$ , and remove the axial diffusion term  $\partial_z^2$  in front of the radial one  $\frac{1}{r} \partial_r (r \partial_r)$ . We then compare the convection and the lateral diffusion terms. Convection dominates if  $Ur^2/DL = \text{Pe}r^2/L^2 = Q/DL \gg 1$  where  $U$  is the mean velocity,  $Q$  is the flow rate,  $D$  is the diffusion coefficient, and  $\text{Pe}$  is the Péclet number defined as  $\text{Pe} = UL/D$ . Taking into account the smallest flow rate  $Q = 10 \mu\text{L h}^{-1}$ , this criterion reads:  $D \ll 1 \times 10^{-10} \text{ m}^2 \text{ s}^{-1}$ . Following Stokes–Einstein equation  $D = k_B T / 6\pi\eta a$ , where  $k_B$  is the Boltzmann constant,  $T$  is the temperature,  $\eta$  is the viscosity of the fluid in which the colloids (or particles, or polymers) are suspended and  $a$  is the hydrodynamic radius of the particle, one can neglect lateral diffusion in our experimental setup for particles with an hydrodynamic radius greater than 2.1 nm. Braschler<sup>28</sup> measured the diffusion coefficient of the alginate under the same conditions and found  $D = 2.44 \times 10^{-11} \text{ m}^2 \text{ s}^{-1}$ . We can thus safely focus on the limit of high Péclet number for the equations describing the alginate and the gel concentrations and we therefore neglect the diffusion of these two species. We however keep it for the evolution of the salt concentration field.

Importantly, we then assume that such a diffusive process does change neither the velocity profiles nor properties of the fluids (viscosity, diffusion rate, ...), which seems fairly legitimate in the case we consider here. Indeed, the viscosity of the jet is already very high compared to that of water; the inner level is thus barely sheared, behaves as a very viscous fluid, and resembles a plug-like flow (as shown in Fig. 2). It will not change much upon gelation. The tracer diffusivity (of salt) in a *dilute* polymer solution or in a cross-linked one is also quite similar. Eventually, the viscosity of the external phase does not depend, in a first approximation, on the concentration of salt. We furthermore neglect the shear-thinning behavior of the alginate solution. In this limit the evolution of the velocity and concentration field are decoupled. We are left with the following sets of equations:

$$\begin{cases} \vec{\nabla} \cdot \vec{v} = 0, \\ \vec{\nabla} P = \vec{\nabla} \cdot \underline{\underline{\sigma}}, \end{cases} \quad (7)$$

and

$$\begin{cases} v_z(r, z) \partial_z [\text{S}] = D_s \frac{1}{r} \partial_r (r \partial_r [\text{S}]) - \xi, \\ v_z(r, z) \partial_z [\text{A}] = -n\xi, \\ v_z(r, z) \partial_z [\text{G}] = \xi, \end{cases} \quad (8)$$

with  $\xi$  calculated by eqn (6).

Underpinned by the solubility product, we expect that the gelation depends on the actual salt concentration: if the solubility product is not reached, the salt concentration evolves through diffusion and the alginate and gel concentrations remain unchanged; when the salt concentration in the internal jet is high enough to reach the solubility threshold, precipitation occurs.<sup>28</sup>

Eventually, we add the initial conditions required to solve the system:

$$\begin{cases} [\text{S}](r < R_i, z = 0) = 0 & \text{and} & [\text{S}](r > R_i, z = 0) = c_{\text{salt}}, \\ [\text{A}](r < R_i, z = 0) = a_0 & \text{and} & [\text{A}](r > R_i, z = 0) = 0, \\ [\text{G}](r, z = 0) = 0 & \text{for all } r, \end{cases} \quad (9)$$

where  $a_0$  is the concentration in monomer (or in  $\text{COO}^-$ ) in the internal jet and  $c_{\text{salt}}$  is the concentration in  $\text{Ca}^{2+}$  in the external layer.

### 4.3 Numerical scheme

To solve this system numerically, we first use dimensionless variables and then proceed *via* a two-step numerical approximation.

The radial size is rendered dimensionless with the size  $R_c$  of the capillary, the velocity with a typical flow velocity  $V = \partial_z P R_c^2 / 4\eta_e$  and the longitudinal distance with  $Z = R_c^2 V / D$ , such as:  $\bar{r} \rightarrow \frac{r}{R_c}$ ,  $\bar{v} \rightarrow \frac{v}{V}$ ,  $\bar{z} \rightarrow \frac{z}{Z}$  and we will omit in the rest the bar to describe dimensionless variables.  $\partial_z P$  is the longitudinal pressure gradient,  $\eta_e$  is the viscosity of the external solution.

As the calculation of the velocity field does not require the knowledge of the concentration profile, we first solve the Stokes equation and find the velocity field. Then, we solve numerically these diffusion–reaction equations to obtain the concentration profile of each species everywhere in the channel.

### 4.4 Velocity field

Due to the hypothesis of cylindrical symmetry, we can calculate an analytical expression for the velocity field by solving the Stokes equation, eqn (7). We do it for each layer, use a non-sliding boundary condition, and get the following velocity profiles:

$$\begin{cases} v_z(r) = m(r^2 - x^2) + (x^2 - 1) & \text{if } 0 \leq r \leq x \\ v_z(r) = (r^2 - 1) & \text{if } x \leq r \leq 1 \end{cases} \quad (10)$$

where  $m = \frac{\eta_e}{\eta_i}$  is the viscosity ratio.

The pressure gradient and the flow rates are related through:

$$\begin{aligned} \partial_z P &= \frac{8\eta_e Q_e}{\pi R_c^4 (1 - x^2)}, \\ x = \frac{R_i}{R_c} &= \sqrt{\frac{\alpha - 1}{\alpha - 1 + m}}, \end{aligned} \quad (11)$$

with  $\alpha = \sqrt{1 + m \frac{Q_i}{Q_e}}$ .

We note that  $xR_c$  is the diameter of the jet and thus the diameter of the obtained wet fibers. Decreasing the flow rate ratio  $Q_i/Q_e$  decreases this diameter. At first sight this formula suggests that fibers as small as wanted may be obtained. We will come back to this point later on in the discussion.

## 4.5 Reaction–diffusion under flow analysis

As the reaction process is much faster than the flow and the diffusion processes, we split the resolution in two steps: first diffusion, then reaction. It permits us to obtain a stable numerical solution, which would not be possible otherwise due to the extreme difference in the (limiting) diffusion and (immediate) reaction kinetics.

The space is discretized (mesh:  $dr$ ,  $dz$ ) and the grid has to be chosen carefully in order to solve the system and to ensure a rapid convergence.<sup>29</sup> We will discuss this point in more detail further.

**4.5.1 Diffusion under flow.** First, we obtain the concentration profile of salt at a point  $z + dz$  knowing the profile at  $z$  by solving numerically the diffusion–convection equation:

$$v(r) \partial_z [\text{S}] = \frac{1}{r} \partial_r (r \partial_r [\text{S}]) \quad (12)$$

where  $v(r)$  is the dimensionless velocity. It yields  $[\text{S}](r, z + dz)$  whatever  $r$  in the chip and the concentrations in alginate and gel are unchanged at this step. After this intermediary step, we denote the concentration  $[\text{S}]^*(r, z + dz)$ ,  $[\text{A}]^*(r, z + dz)$ , and  $[\text{G}]^*(r, z + dz)$  for all  $r$ .

We solve numerically this equation with the following explicit scheme:

$$v(r) \partial_z [\text{S}](r, z) = v(r) \frac{[\text{S}]^*(r, z + dz) - [\text{S}](r, z)}{dz}, \quad (13)$$

$$\frac{1}{r} \partial_r [\text{S}](r, z) = \frac{E}{r dr}, \quad (14)$$

$$\partial_r^2 [\text{S}] = \frac{F}{dr^2}, \quad (15)$$

with

$$\begin{cases} E = [\text{S}](r + dr, z) - [\text{S}](r, z), \\ F = [\text{S}](r + dr, z) - 2[\text{S}](r, z) + [\text{S}](r - dr, z). \end{cases} \quad (16)$$

Thus, eqn (12) becomes:

$$[\text{S}]^*(r, z + dz) = [\text{S}](r, z) + \frac{E dz}{r dr v(r)} + \frac{F dz}{dr^2 v(r)}. \quad (17)$$

This explicit scheme is stable provided the Courant–Friedrichs–Lewy (CFL<sup>29</sup>) condition is checked which requires that  $2dz \ll dr^2 v(r)$  *i.e.*  $dz \ll dr^3$ . In our calculation we use  $dr = 1/200$  and  $dz = 1/(1.5 \times 10^6)$ . Note that in the high Péclet limit  $[\text{A}]^*(r, z + dz) = [\text{A}](r, z)$  and  $[\text{G}]^*(r, z + dz) = [\text{G}](r, z)$ .

**4.5.2 Reaction of gelation.** We use these intermediate data to test whether gelation occurs or not, as predicted by eqn (6). We

recalculate the real concentration of each species for all  $r$  at a distance  $z + dz$  from the nozzle, knowing the concentration field at  $z$  using:

$$\begin{cases} [S](r, z + dz) = [S]^*(r, z + dz) - \xi(r, z + dz), \\ [A](r, z + dz) = [A]^*(r, z + dz) - n\xi(r, z + dz), \\ [G](r, z + dz) = [G]^*(r, z + dz) + \xi(r, z + dz). \end{cases} \quad (18)$$

In that case,  $\xi(r, z + dz)$  is calculated through eqn (6) with the solubility criterion applied on the intermediate concentrations  $[S]^*(r, z + dz)$  and  $[A]^*(r, z + dz)$ .

Upon iteration of these two steps, we obtain the concentration fields everywhere, *i.e.*, for all  $z$  and  $r$  in the channel.

Fig. 6 shows an example of the different concentration fields obtained with this calculation procedure. The upper panel shows cartographies of the concentrations (plane  $r, z$ ) and we observe the output of the model: alginate is consumed upon salt diffusion and the gel is created; note that the boundaries of the alginate and the gel do not move as expected from their neglected diffusion. More precisely, the salt simply diffuses inside the jet until it reaches the solubility limit; at that point, the concentration of alginate decreases at the interface because of the reaction with salt. All the salt above the solubility limit is immediately consumed by the reaction; the salt concentration remains constant until all the monomers have been linked; then the salt concentration increases again, along with its radial progression by diffusion.

Of specific interest for the present study, we recover a documented fact: the gelation front progresses from the outer border of the internal jet to its center.<sup>28</sup> Therefore, in practice when we collect fibers, there is no guarantee that the gel is homogeneous across the section of the jet and we cannot test experimentally this morphological feature; yet, the fibers do have a mechanical rigidity. We thus focus simply on the mean value of the number

of links calculated thanks to our kinetic model. This average is done over the section of the jet at a given distance  $z$  from the nozzle according to the following formula:

$$\rho_{\text{link}}(z) = \frac{2}{R_1^2} \int_0^{R_1} [G](r, z) r dr. \quad (19)$$

We call this quantity *the density of links*. This data provides information about the strength of the gel locally in the device and we will correlate it to our experimental results.

## 5 Discussion

We first extract the solubility product from our measurements and then sort the different states of gel against the calculated density of links.

In order to estimate  $K_s$ , we use the experimental conditions for which there is no gel and run the numerical calculation with the corresponding input parameters (flow rates, salt concentration). We then calculate the density of links at the outlet of the device (at 3 cm from the nozzle) and tune  $K_s$  until we find an ultra-low density of links. While our criterion may seem somewhat arbitrary, we find that  $K_s$  has a strong influence on the link density at the outlet and we eventually converge toward  $K_s \approx 10^{-7}$ . With a finer tuning, we obtain that the link density is still significant for  $K_s = 2 \times 10^{-7}$  while our experiments show no gel, and for  $K_s = 4 \times 10^{-7}$  the link density is negligible while we collect fibers at the outlet of the device. A good compromise is found for  $K_s \approx 3 \times 10^{-7}$ .

Having fixed  $K_s$ , we run the calculation for all the experimental parameters and extract the link density at two locations: near the nozzle (at 1.2 mm from the nozzle) and close to the outlet (at 3 cm from the nozzle). We then construct histograms giving for a specific state (*e.g.*, fiber) the number of occurrences of this state against the density of links that result from the flow and chemical conditions. These histograms are displayed in Fig. 7 for the observation at the outlet level. The ultra-low value for the no-gel condition is a direct consequence of the chosen value of  $K_s$ . In the two cases of pieces-of-gel and continuous fibers, the density of links at the outlet shows a broad yet peaked histogram; beside, the density of links is significantly larger (at least 10 times) than in the absence of gel. Interestingly, the mean number of links is higher *on average* in the situation of pieces-of-gel than in the case of fibers and there are many cases where straight fibers and pieces-of-gel occur for a similar value of the link density. It suggests that the number of links is not the only parameter that controls the morphology, which we discuss below. Eventually, in the case of clogging, the mean density of links is significantly higher than for all other cases.

Table 1 reports the mean value of the link density (dotted line in Fig. 7) for each experimental state and at two positions in the microfluidic chip. We can indeed sort the morphologies on the basis of the link density: in all cases, the gels (fibers or pieces) are formed when the density of links is about ten times higher than at solubility, and clogging also involves about five to ten times more links than for gels; on average, pieces of gel contain more links than the fibers. The same classification holds whether operated near the nozzle or at the outlet, with a larger density of links downstream.

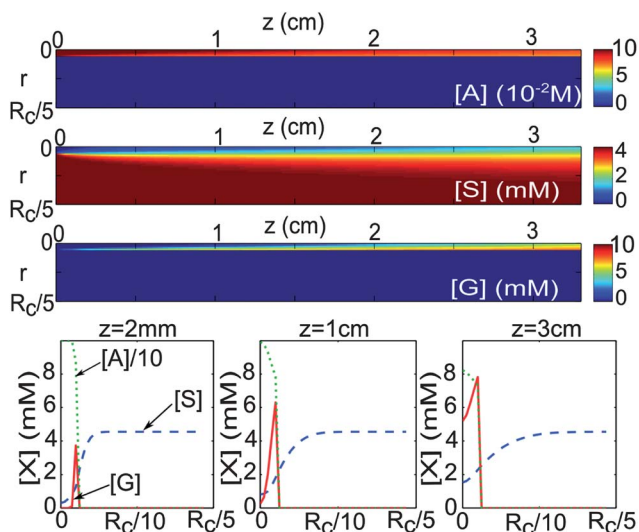


**Fig. 6** Top: concentration field of monomer (top), salt (middle), and gel (bottom) calculated with  $Q_i = 0.01 \mu\text{L s}^{-1}$ ,  $Q_e = 4 \mu\text{L s}^{-1}$ ,  $c_{\text{salt}} = 0.045\%$ ,  $a_0 = 0.1 \text{ mol L}^{-1}$  and  $K_s = 3 \times 10^{-7}$ . Bottom: Radial profiles of concentration for monomer (dotted green line), salt (dashed blue line) and gel (continuous red line) at different distances from the nozzle:  $z = 2$  mm (left),  $z = 1$  cm (middle) and  $z = 3$  mm (right).

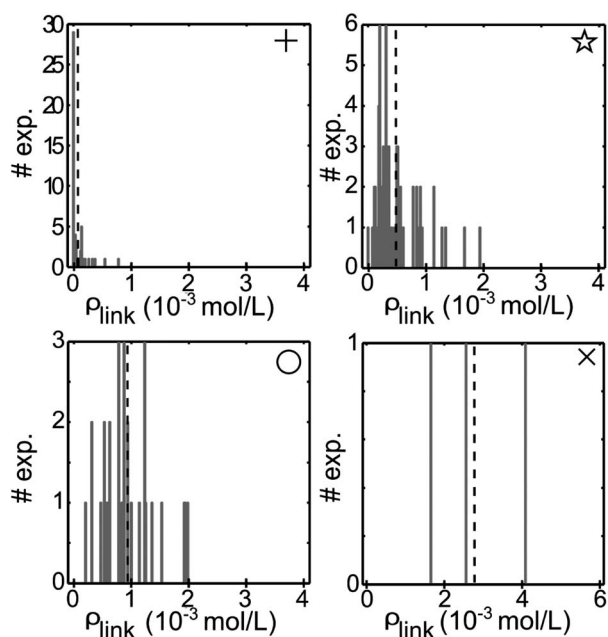


**Fig. 7** Histograms of the density of links  $\rho_{\text{link}}$  calculated at the outlet at 3 cm from the nozzle for the four experimental states (+ no gel,  $\star$  continuous fiber,  $\circ$  pieces of gel,  $\times$  clogging). The dotted line on each diagram corresponds to the mean value of the link density for the considered state; see also Table 1.

**Table 1** Average value of the link density (in  $\text{mol L}^{-1}$ ) calculated at two locations in the chip for every experimental state observed (near the nozzle and at the outlet, at 1.2 mm and 3 cm from the nozzle respectively)

State	$\rho_{\text{link}}$ near the nozzle	$\rho_{\text{link}}$ at the outlet
No gel	$1.0 \times 10^{-5}$	$7.4 \times 10^{-5}$
Continuous fiber	$8.0 \times 10^{-5}$	$4.8 \times 10^{-4}$
Pieces of gel	$1.7 \times 10^{-4}$	$9.4 \times 10^{-4}$
Clogging	$5.3 \times 10^{-4}$	$2.8 \times 10^{-3}$

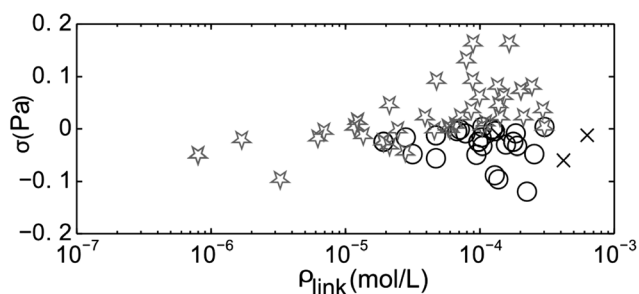


**Fig. 8** Elongational stress exerted on the inner jet at the level of the nozzle as a function of the density of links calculated for the different states obtained experimentally ( $\star$  continuous fibers,  $\circ$  pieces-of-gel,  $\times$  clogging). For clarity reasons, we do not represent experimental cases for which no gel is created.

To go a step further, we introduce a mechanical criterion in order to better discriminate the different states. Indeed, we noticed that some of these states (*e.g.*, pieces-of-gel and clogging) occur near the injection nozzle which is a transient zone for the flow with a component of elongation. The jet is either torn apart

or blocked and to test the impact of the local stress, we calculate it in the focusing zone with a simple dimensional analysis (due to the specific geometry, the exact calculation goes far beyond the scope of our work):

$$\sigma_e = \eta_e \frac{v_u - v}{l} = \eta_e \frac{Q_i}{l} \left( \frac{1}{S_i} - \frac{1}{\pi x^2 R_c^2} \right), \quad (20)$$

where  $v_u$  is the mean velocity in the internal feeding capillary (upstream, before the nozzle),  $v$  is the mean velocity in the jet during the coflow,  $l$  is the length of the focusing zone,  $S_i$  is the section of the internal capillary tube,  $xR_c = R_i$  the radius of the jet after the focusing zone and  $R_c$  is the radius of the external capillary tube. For the sake of simplicity, we consider here that the radius of the internal jet is the one obtained in the absence of gelation with  $x$  given by eqn (11). We also assume that  $l$  is around 3 times the size of the external capillary diameter, *i.e.*,  $l = 1.2$  mm. Note also that  $\sigma_e$  can be positive or negative. When  $\sigma_e > 0$ , the alginate is injected faster than the flow can carry it away so there is compression at the nozzle. Otherwise, there is an elongation at this point. Note that the exact value of  $\sigma_e$  is affected by the flow field and thus by the design of the inlet junction. A T-junction may induce a higher stress than Y-junction.

We report in Fig. 8 the value of the link density  $\rho_{\text{link}}$  near the nozzle for every experimental case as a function of the elongational stress exerted on the internal jet. The correlation is clear and we obtain a new classification for the states. The first obvious observation is that fibers and pieces-of-gel can be roughly differentiated upon the sign of the elongational stress: pieces-of-gel are always created for positive stress whereas fibers mostly occur at a negative stress. We also note that fibers sometimes occur at a very small density of links and we believe that these fibers are actually reticulated downstream, far from the nozzle at a location where there is no elongational stress. It may explain why the sign of the stress at the nozzle is not a discriminant criterion in this precise case. Finally, the zone of clogging is chiefly controlled by the amount of links.

## 6 Conclusions

The fabrication of fibers using a microfluidic device turns out to be delicate. It requires first a well-centered device, which we developed here, in order to reliably control and reproduce the gelation kinetics. Indeed, off-centered devices inevitably induce shape instabilities because of a non-symmetrical gelation. Then, when changing the flow conditions and the cross-linker content, we realized that several states can be generated: no gel, pieces-of-gel, continuous fibers, and clogging. We found that three parameters are adequate to sort experimentally these morphologies: the residence time, the flow rate ratio, and the salt concentration. In the state diagrams we built, the zone of fibers is sometimes rather narrow especially when targeting small diameters. However when the functioning point is well chosen, very long fibers can be easily produced. Typically, for a jet diameter of  $100 \mu\text{m}$  with  $Q_i \approx 50 \mu\text{L h}^{-1}$ , one can produce approximately 6 meters of fiber per hour.

The selection of a given state can be understood from the interplay of two ingredients: the density of links created in the gel and the stress experienced by the jet undergoing gelation. We used a model of reaction–diffusion under flow in order to

calculate this density of links; importantly, the model inputs a solubility product for the gelation which permits initiating gelation only above a certain concentration of the cross-linker. Owing to a few simplifying assumptions, we could generate the density of links for all the states we observed. This density suggests that no gel exists below a certain concentration of cross-linker, that clogging occurs for a very high link density, but is not sufficient alone to discriminate between fibers and pieces-of-gel. Based on the experimental evidence that pieces-of-gel occur from a tear-off mechanism at the nozzle, we used the elongational stress generated in the focusing zone on the jet as an additional mechanical criterion. And indeed, we found that the two gelled states can be differentiated upon the sign of the stress at the nozzle, confirming the intuition. We also noticed that fibers are sometimes produced upon gelation far from the nozzle. There is a last state we omitted to discuss so far: the (rare) case of straight fibers with a diameter which is not tunable with flow rates. Based on our model, we now understand that such a functioning point is peculiar and not reliable because it is too close to the clogging conditions.

An interesting output of this study is the possibility to create pieces-of-gel. They represent the equivalent of drops (emulsions) within the frame of all-miscible fluids and could permit compartmentalizing miscible fluids. In the context of tissue engineering for instance, they might permit creating three-dimensional structures with an original shape, to load them with cells, and to stack them in order to create a scaffold.

However, the most promising output is probably the model and the simplicity with which it permits sorting the states. It might for instance serve as a high-throughput tool to measure solubility products when no gel occurs. It may also help for the fabrication of functional fibers and to control well their size depending on the formulation, which is promising in terms of miniaturization. Finally, it seems exciting to extend our approach beyond the sol-gel reaction we studied here. Any solidification mechanism can be introduced instead of gelation and should permit quantifying the features of the fibers created within these microfluidic devices.

## References

- 1 A. Carlsen and S. Lecommandoux, *Curr. Opin. Colloid Interface Sci.*, 2009, **14**, 329–339.
- 2 J. Cheng, B. A. Teply, I. Sherif, J. Sung, G. Luther, F. X. Gu, E. Levy-Nissenbaum, A. F. Radovic-Moreno, R. Langer and O. C. Farokhzad, *Biomaterials*, 2007, **28**, 869–876.
- 3 G. Talei Franzesi, B. Ni, Y. Ling and A. Khademhosseini, *J. Am. Chem. Soc.*, 2006, **128**, 15064–15065.
- 4 T. Takei, S. Sakai, T. Yokonuma, H. Ijima and K. Kawakami, *Biotechnol. Prog.*, 2007, **23**, 182–186.
- 5 K. H. Bouhadir, K. Y. Lee, E. Alsberg, K. L. Damm, K. W. Anderson and D. J. Mooney, *Biotechnol. Prog.*, 2001, **17**, 945–950.
- 6 N. Lorber, F. Sarrazin, P. Guillot, P. Panizza, A. Colin, B. Pavageau, C. Hany, P. Maestro, S. Marre, T. Delclos, C. Aymonier, P. Subra, L. Prat, C. Gourdon and E. Mignard, *Lab Chip*, 2011, **11**, 779–787.
- 7 P. Guillot, A. Colin, A. S. Utada and A. Ajdari, *Phys. Rev. Lett.*, 2007, **99**, 104502.
- 8 S. Okushima, T. Nisisako, T. Torii and T. Higuchi, *Langmuir*, 2004, **20**, 9905–9908.
- 9 A. S. Utada, E. Lorenceau, D. R. Link, P. D. Kaplan, H. A. Stone and D. A. Weitz, *Science*, 2005, **308**, 537–541.
- 10 J. Thiele, D. Steinhäuser, T. Pfohl and S. Förster, *Langmuir*, 2010, **26**, 6860–6863.
- 11 H. C. Shum, J.-W. Kim and D. A. Weitz, *J. Am. Chem. Soc.*, 2008, **130**, 9543–9549.
- 12 A. Perro, C. Nicolet, J. Angly, S. Lecommandoux, J.-F. Le Meins and A. Colin, *Langmuir*, 2011, **27**, 9034–9042.
- 13 W. J. Lan, S. W. Li, Y. C. Lu, J. H. Xu and G. S. Luo, *Lab Chip*, 2009, **9**, 3282–3288.
- 14 D. Dendukuri, S. S. Gu, D. C. Pregibon, T. A. Hatton and P. S. Doyle, *Lab Chip*, 2007, **7**, 818–828.
- 15 W. Jeong, J. Kim, S. Kim, S. Lee, G. Mensing and D. J. Beebe, *Lab Chip*, 2004, **4**, 576–580.
- 16 S. Shin, J. Y. Park, J. Y. Lee, H. Park, Y. D. Park, K. B. Lee, C. M. Whang and S. H. Lee, *Langmuir*, 2007, **23**, 9104–9108.
- 17 K. H. Lee, S. J. Shin, Y. Park and S.-H. Lee, *Small*, 2009, **5**, 1264–1268.
- 18 E. Kang, S. J. Shin, K. H. Lee and S. H. Lee, *Lab Chip*, 2010, **10**, 1856–1861.
- 19 T. Takei, N. Kishihara, S. Sakai and K. Kawakami, *Biochem. Eng. J.*, 2010, **49**, 143–147.
- 20 B. R. Lee, K. Lee, E. Kang, D.-S. Kim and S.-H. Lee, *Biomechanics*, 2011, **5**, 022208.
- 21 M. Yamada, S. Sugaya, Y. Naganuma and M. Seki, *Soft Matter*, 2012, **8**, 3122–3130.
- 22 C. M. Hwang, A. Khademhosseini, Y. Park, K. Sun and S. H. Lee, *Langmuir*, 2008, **24**, 6845–6851.
- 23 C. H. Choi, H. Yi, S. Hwang, D. A. Weitz and C. S. Lee, *Lab Chip*, 2011, **11**, 1477–1483.
- 24 C. Ouwere, N. Velings, M. Mestdagh and M. A. V. Axelos, *Polym. Gels Networks*, 1998, **6**, 393.
- 25 A. Martinsen, G. Skjak-Braek, O. Smidsrod, F. Zanetti and S. Paoletti, *Carbohydr. Polym.*, 1991, **15**, 171–193.
- 26 W. J. Jeong, J. Y. Kim, J. Choo, E. K. Lee, C. S. Han, D. J. Beebe, G. H. Seong and S. H. Lee, *Langmuir*, 2005, **21**, 3738–3741.
- 27 P. Gacesa, *Carbohydr. Polym.*, 1988, **8**, 161–182.
- 28 T. Braschler, A. Valero, L. Colella, K. Pataky, J. Bruggert and P. Renaud, *Anal. Chem.*, 2011, **83**, 2234–2242.
- 29 R. Courant, K. Friedrichs and H. Lewy, *Math. Ann.*, 1928, **100**, 74–100.